Geomorphology 257 (2016) 10–22

Contents lists available at ScienceDirect

Geomorphology

journal homepage: www.elsevier.com/locate/geomorph

Methodology for classification of geographical features with remote sensing images: Application to tidal flats

G.N. Revollo Sarmiento [a,b,*], M.P. Cipolletti [b], M.M. Perillo [c], C.A. Delrieux [b], Gerardo M.E. Perillo [a,d]

[a] Instituto Argentino de Oceanografía, CONICET-UNS, CC 804, B8000FWB Bahía Blanca, Argentina
[b] Instituto de Investigaciones en Ingeniería Eléctrica, Dpto. de Ing. Eléctrica y de Computadoras, UNS-CONICET, Avenida Alem 1253, Bahía Blanca, Argentina
[c] ExxonMobil Upstream Research Company, Spring, TX, USA
[d] Departamento de Geología, UNS, San Juan 670, Bahía Blanca, Argentina

ARTICLE INFO

Article history:
Received 27 May 2015
Received in revised form 23 December 2015
Accepted 26 December 2015
Available online 30 December 2015

Keywords:
Ponds
Tidal courses
Object detection
Classification
Shape descriptors

ABSTRACT

Tidal flats generally exhibit ponds of diverse size, shape, orientation and origin. Studying the genesis, evolution, stability and erosive mechanisms of these geographic features is critical to understand the dynamics of coastal wetlands. However, monitoring these locations through direct access is hard and expensive, not always feasible, and environmentally damaging. Processing remote sensing images is a natural alternative for the extraction of qualitative and quantitative data due to their non-invasive nature. In this work, a robust methodology for automatic classification of ponds and tidal creeks in tidal flats using Google Earth images is proposed. The applicability of our method is tested in nine zones with different morphological settings. Each zone is processed by a segmentation stage, where ponds and tidal creeks are identified. Next, each geographical feature is measured and a set of shape descriptors is calculated. This dataset, together with a-priori classification of each geographical feature, is used to define a regression model, which allows an extensive automatic classification of large volumes of data discriminating ponds and tidal creeks against other various geographical features. In all cases, we identified and automatically classified different geographic features with an average accuracy over 90% (89.7% in the worst case, and 99.4% in the best case). These results show the feasibility of using freely available Google Earth imagery for the automatic identification and classification of complex geographical features. Also, the presented methodology may be easily applied in other wetlands of the world and perhaps employing other remote sensing imagery.

1. Introduction

Estuaries are dynamic systems subject to a wide variety of geographical and temporal variations. In estuaries, tidal flats are environments with unconsolidated sediments and without vascular vegetation, which are normally exposed during low tide. Understanding the evolution of geographical features in estuaries is essential to determine the dynamic processes that occur in coastal wetlands (Perillo et al., 2009). This is especially true for ponds and tidal courses as proposed by Perillo (2009) that are among the most significant physiographic features in salt marshes and tidal flats (Chapman, 1960).

Ponds were first described and categorized by Yapp et al. (1917) as depressions on the surface of a salt marsh where water may or may not be retained after tidal inundation (Perillo and Iribarne, 2003). Despite many studies and genetic theories (Steers, 1964; Packham and Liddle, 1970; Pethick, 1974; Boston, 1983; Frey, 1985; Perillo et al., 1996; Perillo and Iribarne, 2003), there is no consensus on what are the geomorphological processes controlling their formation and evolution. This is due to the difficulty in obtaining reliable data without modifying their natural condition and thus their evolution. The real causes of their origin is still under discussion, mostly because there are several independent processes that affect the ponds' formation mechanisms, such as interaction of plants and benthic fauna which are seldom described in the literature (Minkoff et al., 2006; Escapa et al., 2015). So far, there has been no significant research results of this type in tidal flats. Moreover, it is likely that formation mechanisms could be quite different between tidal flats and salt marshes, and the way they evolve as well.

Considering the disadvantages of direct in situ monitoring (i.e., the high costs and difficulties associated with the deployment of a research team and equipment, and the damaging influence to the natural environment), a sensible alternative is to use techniques that do not exert a negative influence on the areas, such as the use of aerial or satellite images. In contrast to on site observation, remote sensing includes a set of techniques aimed to acquire information

* Corresponding author at: CC804, B8000FWB Bahía Blanca, Argentina.
E-mail addresses: giselarevollo@gmail.com (G.N. Revollo Sarmiento), mpcipolletti@gmail.com (M.P. Cipolletti), mauricio.m.perillo@exxonmobil.com (M.M. Perillo), cad@uns.edu.ar (C.A. Delrieux), gmeperillo@criba.edu.ar (G.M.E. Perillo).

http://dx.doi.org/10.1016/j.geomorph.2015.12.020
0169-555X/

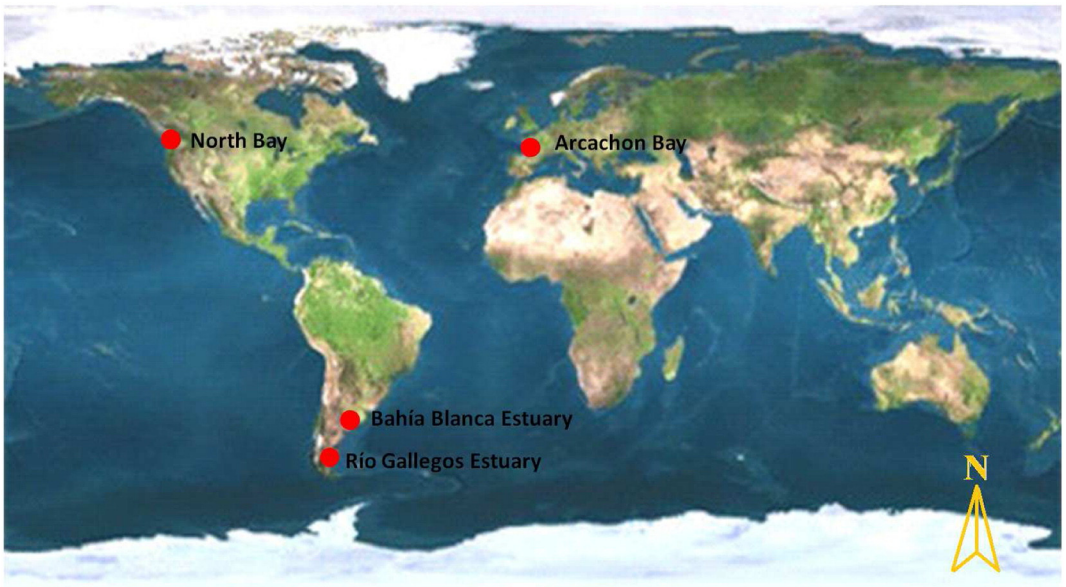

Fig. 1. Distribution of the study areas. Bahía Blanca Estuary: Zone 1: (39°1.228′S,62°9.676′W). Zone 2: (39°0.178′S,62°8.718′W). Zone 3: (39°0.126′S,62°8.719′W). Zone 4: (39°0.181′S,62°8.579′W). Zone 5: (39°1.201′S,62°9.786′W). Río Gallegos Estuary: Zone 6: (51°38.063′S,69°3.342′W). Zone 7: (51°37.158′S,69°3.342′W). North Bay (USA)(Zone 8): (47°0.939′N,124°6.145′W). Arcachon Bay (France)(Zone 9): (44°42.768′N,1°7.171′W).

about objects or phenomena, without requiring physical contact, since the sensors rely on propagated signals (typically electromagnetic radiation) (Campbell, 2002; Lillesand et al., 2004; Richards and Jia, 2006). Digital Image Processing (DIP) applied to remote sensing imagery may provide useful information and understanding of different features and geographical characteristics of the Earth and, in our case, the quantification of ponds and tidal courses and their interaction in coastal areas.

Data classification in remote sensing images is a complex process, despite of great advances in developing different techniques to achieve adequate accuracy (Franklin et al., 2002; Pal and Mather, 2003; Gallego, 2004). Classifying remotely sensed data into a specific thematic remains a challenge because many factors (i.e., sensor modalities, selected remotely sensed data, image processing, etc), and underlying assumptions rely on different methodologies of classification. At the present time, Digital Globes imagery (e.g. Google Earth) is a useful tool in Earth Science research (Friess et al., 2011; Yu and Gong, 2012; Zular et al., 2012) due to its free global coverage with high spatial resolution imagery.

There are just a few research results that analyze the formation and identification of ponds by remote sensing data sets, including aerial or satellite images (Sridhar et al., 2008; Goudie, 2013). However, the methodological aspects (i.e., segmentation, measurement and classification of ponds) require a fair amount of human supervision. In fact, this is a complex and time-consuming task that requires several specific skills.

The aim of this article is to present a methodology for automatic classification of ponds and tidal courses in tidal flats using remote sensing images. The main stages involve segmentation, measurement, extraction of morphological parameters and automatic recognition of objects under study using DIP techniques. In this sense, this work provides useful information allowing human intervention to focus on the interpretation of these data sets rather than the time-consuming manual analysis of the image features. In fact, the data contribute to testing hypotheses on the formation, importance, relation between ponds and tidal courses and to understand how these features affect the morphology of tidal flats. The method is relatively simple and can be readily applied to coastal wetlands worldwide employing either Google Earth (GE) images or any other image that have similar features. Multi-and hyperspectral images may allow much more refined results as shown in previous works (Cipolletti et al., 2012; Cipolletti et al., 2014). At the present status of our research, we can not provide yet definitions as to what processes actually form the ponds and their relationship with the geomorphology

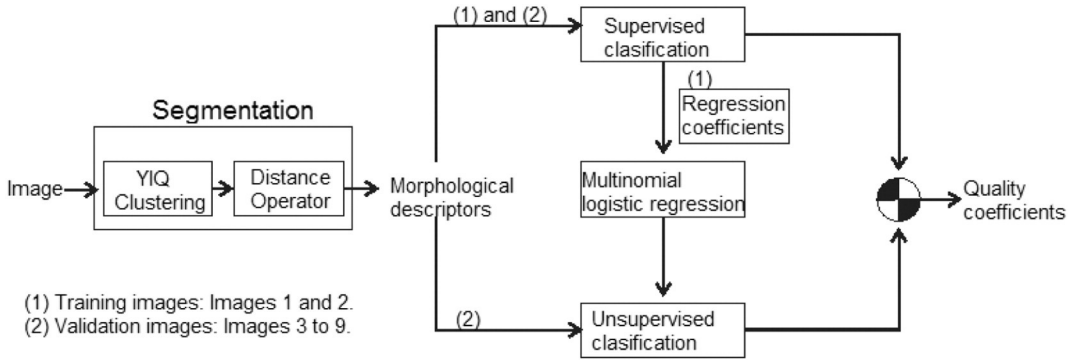

Fig. 2. Complete processing pipeline for detection of geographic features: preprocessing and classification.

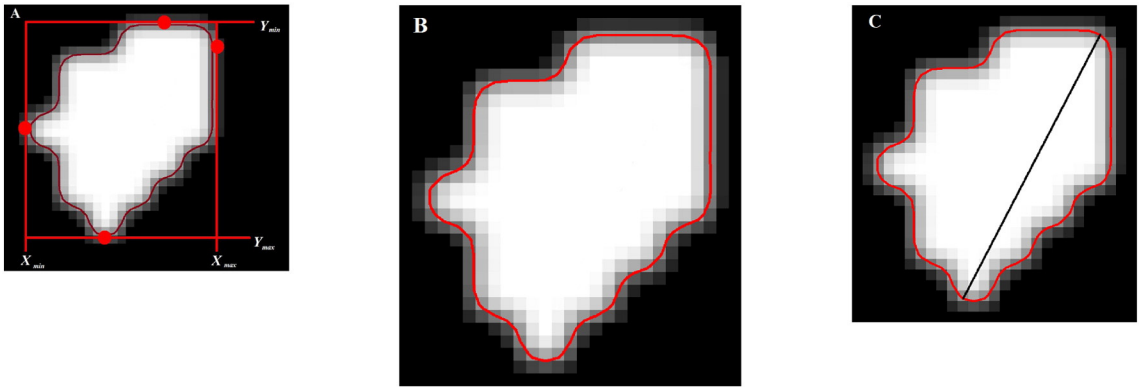

Fig. 3. Shape descriptors. 2 Minimax box, 2 Border extraction using Marching squares with linear interpolation, 2 Feret diameter.

and dynamic conditions prevailing on the areas where they are found.

2. Materials and methods

2.1. Study area and sample preparation

Nine zones with different geomorphological settings located in different estuaries and bays were carefully chosen previous to a detailed analysis of the pond features existing in those areas (Fig. 1). On one hand, the Bahía Blanca Estuary, located in the Southwestern Atlantic, is a typical example of coastal environment with tidal flats worldwide (i.e., Bay of Fundy, Gallegos Estuary, Arachon Bay) presenting ponds of different sizes, shapes and orientations. In this context, prior to a detailed analysis of pond features existing in this estuary, five zones were selected. On the other hand, four geographical areas in different bays and estuaries worldwide were selected. These sites have similar features of ponds and tidal courses in tidal flats as in Bahía Blanca Estuary.

Google Earth images were used to extract quantitative and qualitative information employing DIP techniques. These images are arrays of RGB pixels, plus their spatial reference, which come in a wide range of spatial resolutions specified in the copyright information. Most land areas have 15 m resolution, but the most detailed GE images can have resolutions as fine as 15 cm. In this way, information in raster format is provided and can be integrated with existing layers into a Geographic Information System (GIS) through data processing.

In particular, to identify the geographic features under study, frames of 930 × 509 pixels were used to sample the tidal flat. These frames were exported from the GE application as images; the virtual altitude was set to 290 m, which corresponds to a geographic extents of 360 × 174 m per frame. This scale was an adequate trade-off between level of detail and coverage, and was also used to measure pixel size ($1 pixel = 0.3$ m). Different dates of imagery were used because GE images have changed over time (i.e., time that satellites captured the images, tide and weather conditions). For instance, the Bahía Blanca images were captured on March 18, 2011, Arcachon and North Bay on August 7, 2012 and September 4, 2011, respectively. Finally, Río Gallegos images correspond to January, 2013.

The processing methodology was developed using Qt Creator IDE and OpenCV (Open Source Computer Vision Library). This consists of two stages, preprocessing and classification (Fig. 2). However, the processing pipeline can easily be developed in other softwares (i.e., Matlab, Delphi, Java, Python, etc).

2.2. Preprocessing

The preprocessing stage involves the segmentation, feature extraction and measurement, and morphological descriptors modules. The development of these modules is now introduced. The segmentation algorithm operates in the YIQ color space, which splits luminance (Y) from chromaticity (IQ) (Girard and Girard, 1999; Richards and Jia, 2006). It is based on a previous clustering of color attributes of foreground and background features, and establishing a distance operator among these clusters. The goal is to distinguish ponds and tidal courses (foreground) from the rest of the image (background).

The usual segmentation strategy consists of manually selecting significant groups of foreground and background pixels (representative pixels) through expert judgment. These later are picked up from the center of features of interest, then their respective prototype colors in color space (i.e., as a weighed average of the selected pixels) is

Table 1
Shape descriptors and their analytical definition.

Name	Symbol	Math definition
Box area	A_{box}	$(x_{\max}\text{-}x_{\min})*(y_{\max}\text{-}y_{\min})$
Form factor	ff	$\frac{4\pi A}{P^2}$
Roundness	rd	$\frac{4A}{\pi\|\|LD\|\|^2}$
Extent	ex	$\frac{A}{A_{box}}$
Compactness	cp	$\frac{\sqrt{\frac{4}{\pi}A}}{\|\|LD\|\|}$

Table 2
Performance matrix. (A) Confusion matrix. (B) Quality standard terms.

A

		Predicted		
		Negative	Positive	Total
Actual	Negative	Tn	Fp	$An = Tn + Fp$
	Positive	Fn	Tp	$Ap = Fn + Tp$
	Total	$Pn = Tn + Fn$	$Pp = Fp + Tp$	T

B

Definition	Symbol	Math definition
Global Accuracy	A_g	$Tn + Tp/(An + Ap)$
True positive rate	R_{Tp}	Tp/Ap
True negative rate	R_{Tn}	Tn/An
False negative rate	R_{Fn}	Tn/Pn
False positive rate	R_{Fp}	Tp/Pp
Auxiliary parameter	$P_r(a)$	$(Tn + Tp)/T$
Auxiliary parameter	$P_r(e)$	$(An^*Pn + Ap^*Pp)/T^2$
Cohen's kappa coefficient	κ	$P_r(a)\text{-}P_r(e)/(1\text{-}P_r(e))$

established and, finally, every pixel in the image is classified either as foreground or background according to the closest distance in color space between the color of the pixel and the color of the prototypes (Friedman and Rubin, 1967; Haralick and Kelly, 1969; Saha and Bandyopadhyay, 2010). However, in these particular images this simple idea is doomed to fail due to the high color dispersion of the representative pixels. An inspection of the color distribution of the representative pixels in Y vs. I plane suggests that a different strategy is in order. A polygonal can be determined which splits the Y vs. I plane in two regions, one containing the color of all foreground representative pixels, and the other containing the color of the background representative pixels. With this delimitation, it is possible to devise a method for classifying every pixel as either foreground or background. This 'multi-distance' algorithm selects manually two groups of prototype pixels of each zone: r_i^f and r_j^b, belonging to foreground and background, respectively. Then, computes D over every pixel in the original image, applying Eq. (1), based on the selection of r_i^f and r_j^b prototype pixels. The subscript i/j indicates the i/j-th foreground/background representative pixel, which ranges from $1 \le i \le F / 1 \le j \le B$, where F and B are the total number of representative pixels in each class. The multi-distance operator is defined as:

$$\begin{aligned} d_i^f &= \sqrt{\left(x_Y - r_{(i)Y}^f\right)^2 + \left(x_I - r_{(i)I}^f\right)^2}, \\ D^f &= \min_{1 \le i \le F}\left(d_i^f\right) \\ d_j^b &= \sqrt{\left(x_Y - r_{(j)Y}^b\right) + \left(x_I - r_{(j)I}^b\right)^2} \\ D^b &= \min_{1 \le j \le B}\left(d_i^b\right) \end{aligned} \tag{1}$$

where x_Y and x_I indicate Y,I pixel components, $r_{(i)Y}^f$ and $r_{(i)I}^f$ indicate Y,I components of the i-th foreground representative pixel and, $r_{(j)Y}^b$ and $r_{(j)I}^b$ indicate Y,I pixel components of the j-th background representative pixel. Each pixel of the image is then classified as foreground if $D^f \le D^b$ or background if $D^f > D^b$.

After this segmentation process, the foreground of the resulting binary image contains a set of connected regions, each representing the segmentation of a single geographic feature (either a pond, a tidal

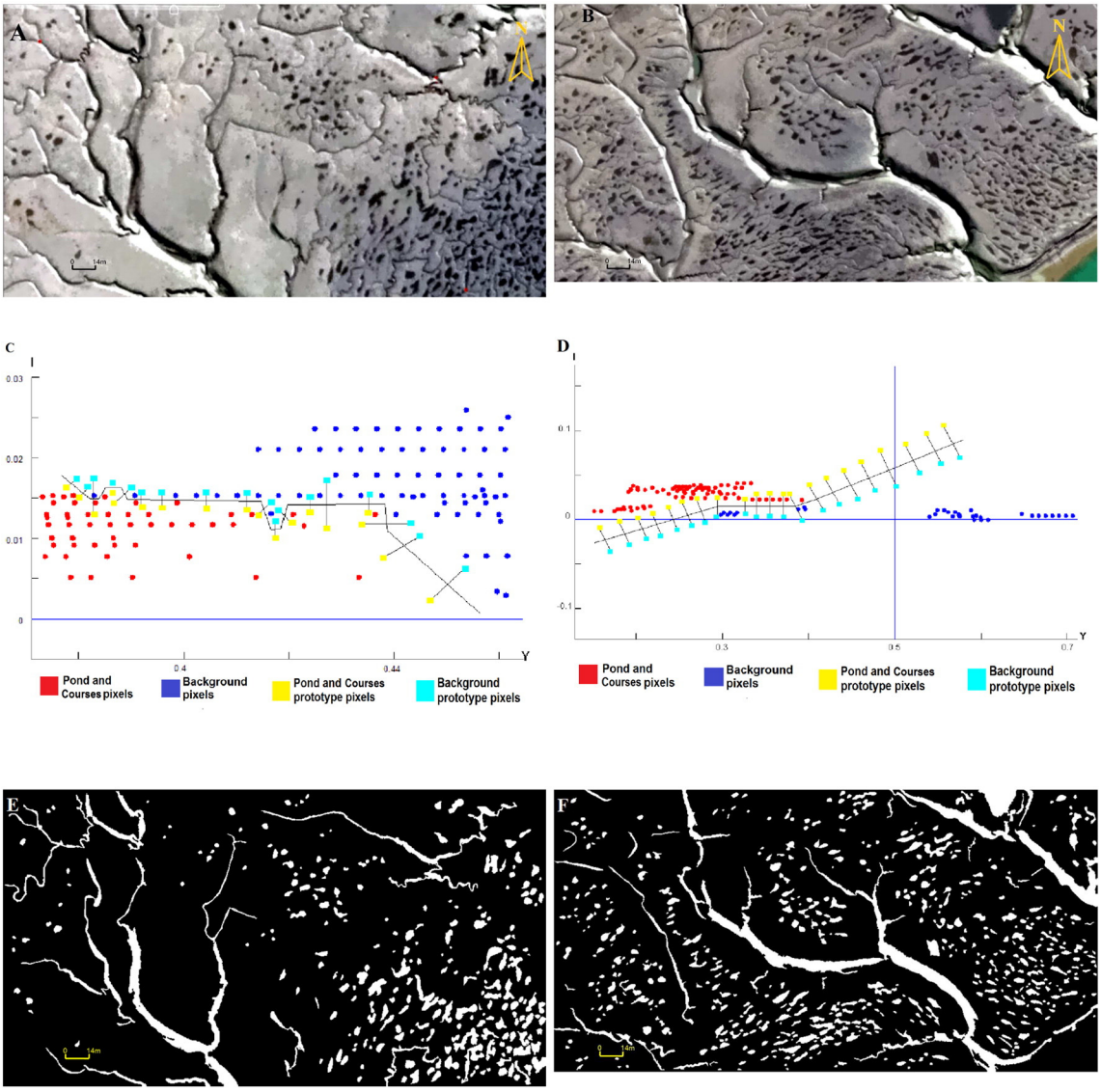

Fig. 4. Bahía Blanca Estuary training zones. (A) Zone 1. (B) Zone 2. Color distribution of the representative pixels in Y vs. I plane, where foreground and background pixels are red and blue, respectively, prototype pixels are in yellow (r^f) and cyan (r^b) in zones (C) 1 and (D) 2. Binary images, where background and foreground pixels are black and white, respectively, zones (E) 1 and (F) 2. (For interpretation of the references to color in this figure legend, the reader is referred to the web version of this article.)

creek, or a spurious structure). Then, the next processing step is aimed at recognizing each region accordingly, using a supervised shape analysis procedure.

The perimeter (P) is measured using the Marching Squares algorithm with linear interpolation MSI (Cipolletti et al., 2012) (Fig. 3). In order to approximate the contour shape by a polygon with variable-length segments, a low-pass Gaussian convolution filter is applied to the binary image to create a gray scale image. Then, the coordinates of each segment allow to extract the end points (Fig. 3A) and the Feret diameter with module and angle (i.e., longest diagonal $||LD||$ and LD_ϕ, Fig. 3C). The net area (A) is calculated by the MSI method. Finally, several shape descriptors are calculated: form factor (ff), roundness (rd), extent (ex), box area (A_{box}) and compactness (cp) (Russ, 1999) (Table 1).

2.3. Classification

The supervised training of a classifier and the design of a statistical regression model are performed in this second stage. This step requires a supervised intervention that discriminates each geographic feature (ponds, tidal courses, etc.) by class. The supervised training is performed using three classes: ponds (P), courses (C) and various structures or 'other' (O). With this labeled and using the available data (shape descriptors) obtained in preprocessing stage, we developed a regression model allowing for automatic classification. The class O contains a set of connected regions that are others geographic features that do not purely correspond to ponds or tidal courses for reasons of dynamic sediment to tidal course or pond.

A multinomial logistic regression (Hosmer and Lemeshow, 2000) is performed using the MATLAB (R2012a) Statistics Toolbox. Multinomial logistic regressions are one of the most common tools to analyze categorical data (Agresti, 1996). Thus, considering 1507 observations (zones 1 and 2 features) as the sample size, three different types of morphologies Pond (P), Course (C) and Other (O) are defined as the categorical variables with the shape descriptors (Table 1) as the independent variables

$$\begin{aligned} P &= f_1(ff_i, ex_i, cp_i, rd_i, A_{box,i}) \\ C &= f_2(ff_i, ex_i, cp_i, rd_i, A_{box,i}) \\ O &= f_3(ff_i, ex_i, cp_i, rd_i, A_{box,i}). \end{aligned} \tag{2}$$

The multinomial logistic regression uses a linear function $f(k,i)$ to predict the probability that the observation i has outcome k, using the following form:

$$\begin{aligned} X_i &= (ff_i, ex_i, cp_i, rd_i, A_{box,i}) \\ f(k,i) &= \beta_{0,k} + \beta_{1,k}x_{1,i} + \cdots + \beta_{M,k}x_{M,i}, \\ f(k,i) &= \beta_k \cdot X_i, \\ \ln \frac{\Pr(Y_k)}{\Pr(Y_K)} &= \beta_k X_i \end{aligned} \tag{3}$$

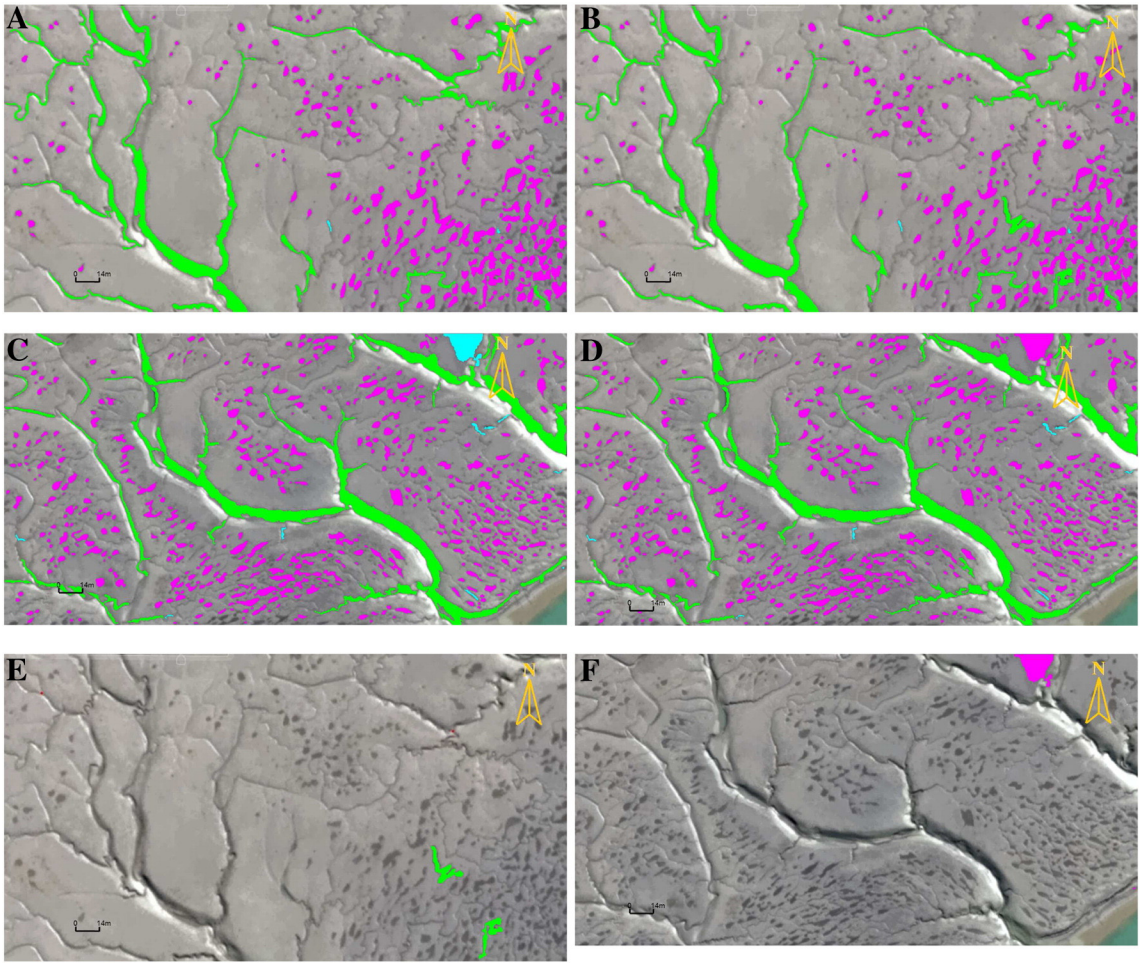

Fig. 5. Classification results in Bahía Blanca Estuary training zones with their global accuracy. Zone 1: 4 Supervised Classification-$A_g = 100\%$. 4 Automatic Classification-$A_g = 99.2\%$. Zone 2: 4 Supervised Classification-$A_g = 100\%$. 4 Automatic Classification-$A_g = 99.4\%$. Pond, Course and Other classes are shown in magenta, green, and cyan, respectively. Classification error: 4 Ponds classified as tidal course in Zone 1. 4 Other structure classified as Pond in Zone 2.

where β_k is the set of regression coefficients associated with the k-th class and $X_i = (X_{1,i}\ldots,X_{m,i})$ is the set of explanatory variables associated with observation i. Then, for K possible outcomes, there are K-1 independent binary logistic regression models, in which one class is chosen as a 'pivot' and, then, the other K-1 outcomes are separately regressed against the pivot outcome K. If we exponentiate both sides and solve for the probabilities, then:

$$\Pr(Y_k) = \Pr(Y_K)e^{\beta_k X_i}.$$

Using the fact that all K probabilities must sum to one, this results in:

$$\mathcal{P}_{Y_K} = \Pr(Y_K) = \frac{1}{1 + \sum_{k=1}^{K-1} e^{\beta_k X_i}} \quad (4)$$

and the other probabilities are:

$$\mathcal{P}_{Y_k} = \Pr(Y_k) = \frac{e^{Z_{k,K}}}{1 + \sum_{k=1}^{K-1} e^{\beta_k X_i}}. \quad (5)$$

2.4. Performance analysis

The ability of the model to classify geographic features is related to its accuracy. In this case, a qualitative and quantitative evaluation is performed as metric. The former is based on expert knowledge.

For instance, the confusion matrix or matching matrix is the most used approach to estimate the performance of the model (Foody, 2002; Lunetta and Lyon, 2004; Congalton and Green, 2008). The confusion matrix summarizes the data of the total number of features against data obtained from unsupervised classification (Table 2B). In addition, several parameters are calculated from the confusion matrix (Table 2B) to estimate the accuracy depending on the total of the studied features (T). Global accuracy (A_g) quantifies the number of features correctly classified. Classes accuracy, which is the proportion of true positive and negative rates (R_{Tp} and R_{Tn}), shows the percentage of features belonging to the k-th class correctly classified.

Allocation accuracy is the proportion of false positive and negative rate (R_{Fp} and R_{Fn}) and shows the percentage of features classified as 'k' class that really belong to that class. R_{Fp} and R_{Fn} are associated with 'allocation' and 'omission' errors, respectively. Furthermore, these kinds of errors quantify the number of features classified as the 'k-th' class that belongs to another, and the number of features corresponding to the 'k-th' class that were not correctly classified.

Another popular metric is the Kappa coefficient (κ) (Cohen, 1960; Congalton, 1991; Wilkinson, 2005). This coefficient is a consensus measurement among two opinions. In this sense, κ has become a standard accuracy assessment in the remote sensing literature (Congalton and Green, 2008), despite some criticisms (i.e., κ is a ratio, which can introduce problems in calculation and has no useful interpretation) (Jr et al., 2011).

3. Results

This robust multi-estuary study tested the applicability of our method in different geomorphological settings. The overall zones were carefully chosen as the most representative of pond diversity. Considering the Bahía Blanca geographic features as representative in tidal flats worldwide, zones 1 and 2 were used to train the supervised classifier while the other set of zones (3 to 9) were employed to validate the accuracy of the method.

All zones are preprocessed and then classified manually through expert judgment. Then, the unsupervised classifier is applied in zones 3 to 9 and its performance is assessed. The results of the supervised classification are compared against the results of the unsupervised classification to evaluate the accuracy of the method.

3.1. Results from the training images

Fig. 4 displays the segmentation results, YIQ clustering, and foreground/background prototype pixels (r_i^f and r_j^b) separated by the polygonal in a the scatter plot Y vs. I (Fig. 4E, F) and its binary images (Fig. 4C, D). The foreground pixels contains ponds, tidal courses and other structures, the latter being geographical features that do not purely correspond to these.

The class O (various structures) is used as pivot in the linear model experimental data. Following the Eq. (3) the two associated log-odds or logits are:

$$Z_{C,O} = 15.5\,ff - 4.3\,ex - 1.1\,cp - 5\,rd + 5.5\,A_{box} - 8.2 \quad (6)$$

and

$$Z_{P,O} = 7.7\,ff + 1.1\,ex - 68.3\,cp + 43.4\,rds + 5.3\,A_{box} + 10.7, \quad (7)$$

where -8.2 and 10.7 are two constants and the rest of the values are the regression coefficients computed from the model. The R^2 of the regression coefficient is 0.65 and the average p-value is 0.02. Despite the

Table 3
Bahía Blanca Estuary Zone 1 performance: (A) Confusion matrix. (B) Classification results. Bahía Blanca Estuary Zone 2 performance: (C) Confusion matrix. (D) Classification results.

A

		Predicted		
		Pond	Course	Other
Actual	Pond	225	2	0
	Course	0	12	0
	Other	0	0	2

B

Parameter	Value
A_g[%]	99.2
True ponds rate (R_{Tp})	0.99
True courses rate (R_{Tc})	1.00
True others rate (R_{To})	1.00
False ponds rate (R_{Fp})	1.00
False courses rate (R_{Fc})	0.85
False others rate (R_{Fo})	1.00
$P_r(a)$	0.99
$P_r(e)$	0.88
κ	0.93

C

		Predicted		
		Pond	Course	Other
Actual	Pond	486	1	0
	Course	0	25	0
	Other	2	0	10

D

Parameter	Value
A_g[%]	99.4
R_{Tp}	0.99
R_{Tc}	1.00
R_{To}	0.83
R_{Fp}	0.99
R_{Fc}	0.96
R_{Fo}	1.00
$P_r(a)$	0.99
$P_r(e)$	0.86
κ	0.95

relatively low R^2, the fact that the p-value is less than 0.05 allows the rejection of the null hypothesis, thus making the regression statistically significant. These logits, Eqs. (6) and (7), are used to formulate a probabilistic model to obtain the likelihood of categorical variables (ponds, course and others) for an individual set of shape descriptors in Eqs. (4) and (5):

$$\mathcal{P}_O(ff, ex, cp, rd, A_{box}) = \frac{1}{1 + e^{Z_{C,O}} + e^{Z_{P,O}}}, \tag{8}$$

$$\mathcal{P}_C(ff, ex, cp, rd, A_{box}) = \frac{e^{Z_{C,O}}}{1 + e^{Z_{C,O}} + e^{Z_{P,O}}}, \tag{9}$$

$$\mathcal{P}_P(ff, ex, cp, rd, A_{box}) = \frac{e^{Z_{P,O}}}{1 + e^{Z_{C,O}} + e^{Z_{P,O}}}. \tag{10}$$

Hence, in both zones, the statistical model is computed and afterwards taken as the base for the unsupervised classifier. In particular, A_g and the κ coefficient in zone 1 are 99.2% and 0.93, and in zone 2 99.4% and 0.95, respectively. The contrast between supervised vs. unsupervised classification is shown in Fig. 5. The confusion matrix and accuracy parameters are detailed in Table 3.

In general, accuracy values R_{Tp}, R_{Tn} and R_{To} are higher than 0.8, then a high hit ratio is assumed (Table 3). $R_{Tp} = 0.99$ in Zone 1 reveals a minimum learning error, few ponds are confused with tidal courses (Fig. 5E) because their feature variability. Nevertheless, there are not false positives ($R_{Fc} = 1.00$) in class *C*. The κ coefficient displays a high proportion of matches between both classifications (supervised and unsupervised) and, according to (Fleiss, 1981), the consensus between supervised and unsupervised classification obtained in the training zones is optimal.

3.2. Results from validation images

The model was tested on the second set of images, (zones 3 to 9). Figs. 6, 7 and 8 show the supervised vs. unsupervised classification results. A_g coefficients in zones 3 to 5 are 96.6, 95.9 and 96.3%, respectively, while κ coefficients are 0.84, 0.58 and 0.80, respectively. In zones 6 to 9, the values of A_g are 89.7, 97.8, 91.4 and 94.5%, respectively, and κ coefficients are 0.7, 0.95, 0.7 and 0.8, respectively.

In particular, A_g values are higher than 89% in all different geomorphological settings. The confusion matrix and accuracy parameters for each zone are detailed in Tables 4, 5 and 6.

Accuracy values, R_{Tp} and R_{Tc}, are higher than 0.90 in the validation zones. In particular, in zones 4 to 8 the R_{Tc} equals 1, which shows that there is no learning error because segmentation does not have remnants of the main tidal courses. However, in zones 3 and 4, the R_{To} obtained are relatively low, 0.59 and 0.42, because the *O* class features are similar in shape to ponds. Fig. 6E and F displays false positives (other structures classified as ponds and ponds classified as other structures). κ coefficients, according to

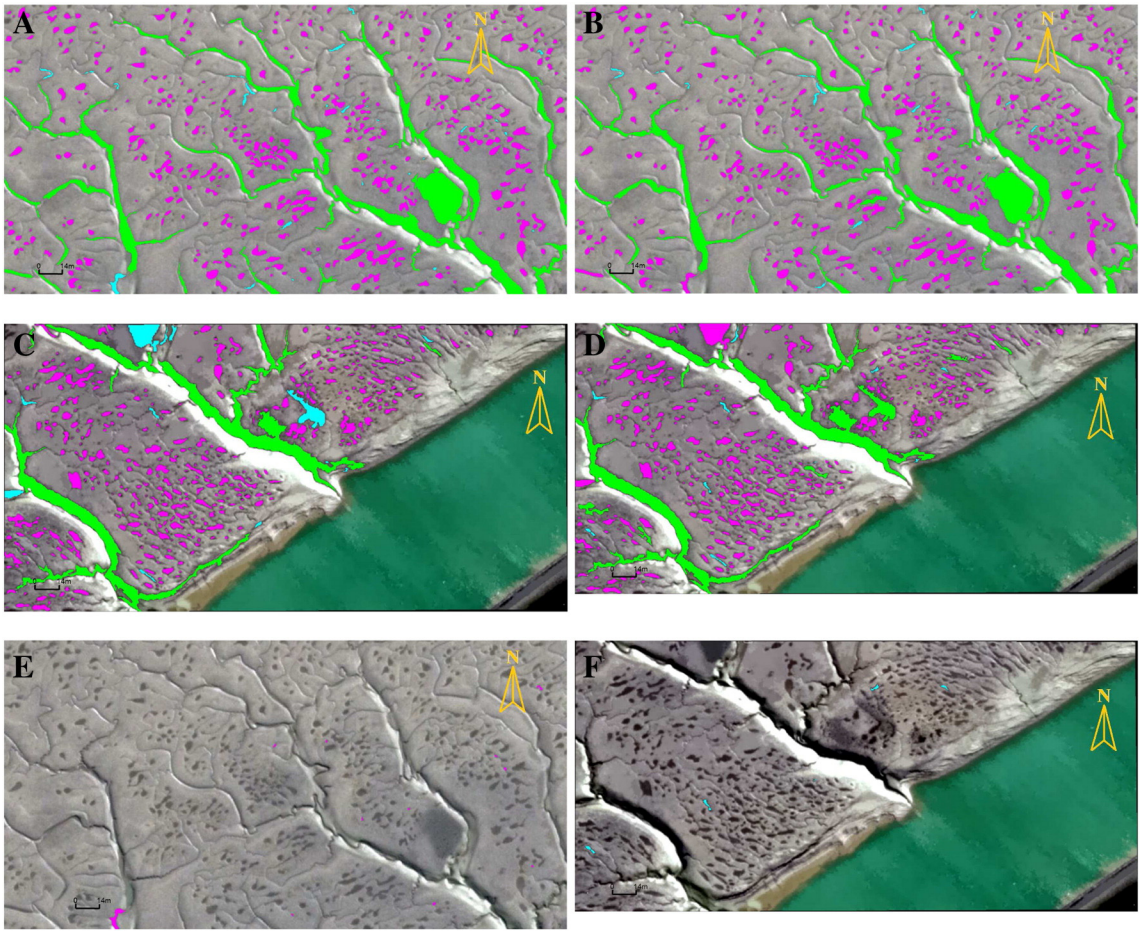

Fig. 6. Classification results in Bahía Blanca Estuary validation zones with their global accuracy. Zone 3: 5 Supervised classification-$A_g = 100\%$. 5 Automatic classification-$A_g = 96.6\%$. Zone 4: 5 Supervised classification-$A_g = 100\%$. 5 Automatic classification-$A_g = 95.9\%$. 5 Other structures classified as ponds in Zone 3. 5 Ponds classified as other structures in Zone 4. Pond, Course and Other classes are shown in magenta, green and cyan, respectively.

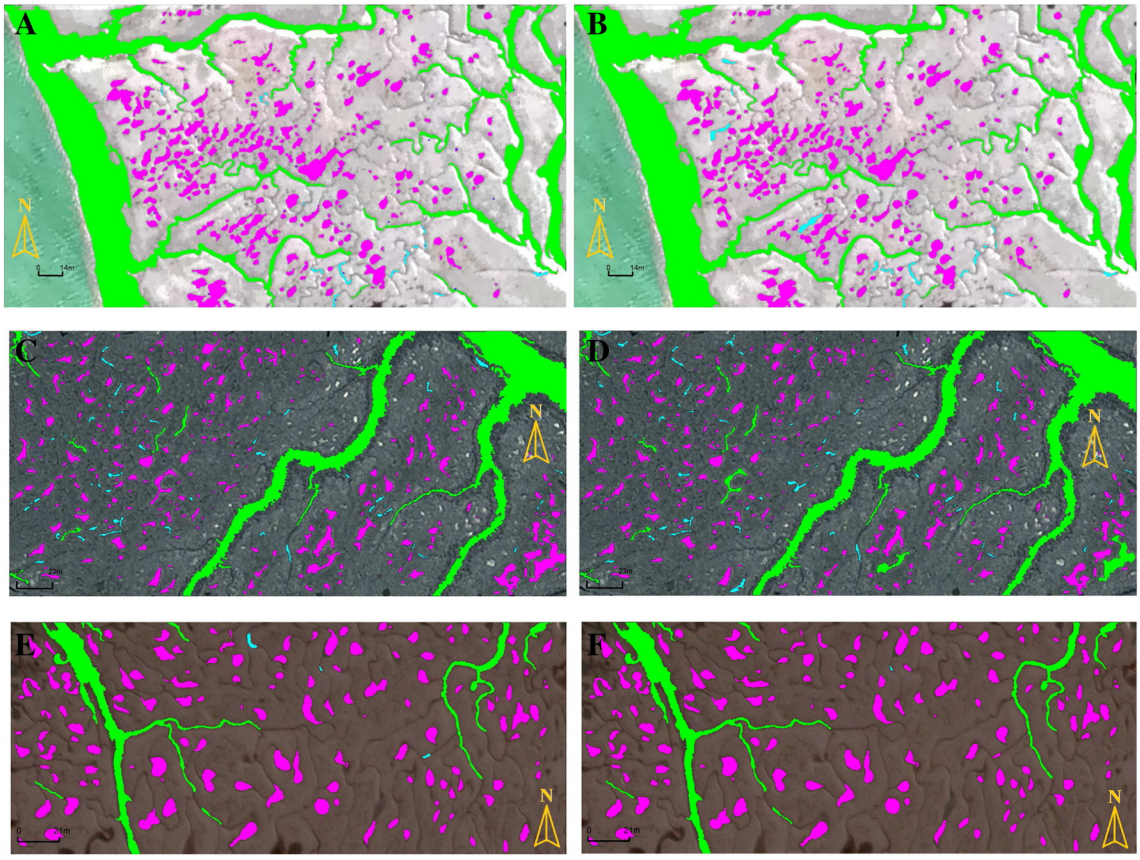

Fig. 7. Classification results in validation zones with their global accuracy. Bahía Blanca Estuary Zone 5: 6 Supervised classification-$A_g = 100\%$. 6 Automatic classification-$A_g = 96.3\%$. Río Gallegos Estuary Zone 6: 6 Supervised classification-$A_g = 100\%$. 6 Automatic classification-$A_g = 89.7\%$. Río Gallegos Estuary Zone 7: 6 Supervised classification-$A_g = 100\%$. 6 Automatic classification-$A_g = 97.8\%$. Pond, Course and Other classes are shown in magenta, green and cyan, respectively.

(Fleiss, 1981) is good in zone 4, and optimal in remaining zones. In all zones, ponds are the most frequent structure (i.e., the classes are significantly unbalanced).

In Figs. 9 and 10, we use mosaic plots (Hartigan and Kleiner, 1981; Friendly, 1994) to show graphically the confusion matrices. In this regard, the relation between the success and failure ratio of the automatic classification is shown in red and yellow, respectively.

In general, the classification confidence level (A_g) is over 89% and clearly the *P* class is predominant at a rate greater than 54%. In contrast, the presence of tidal courses is the least frequent

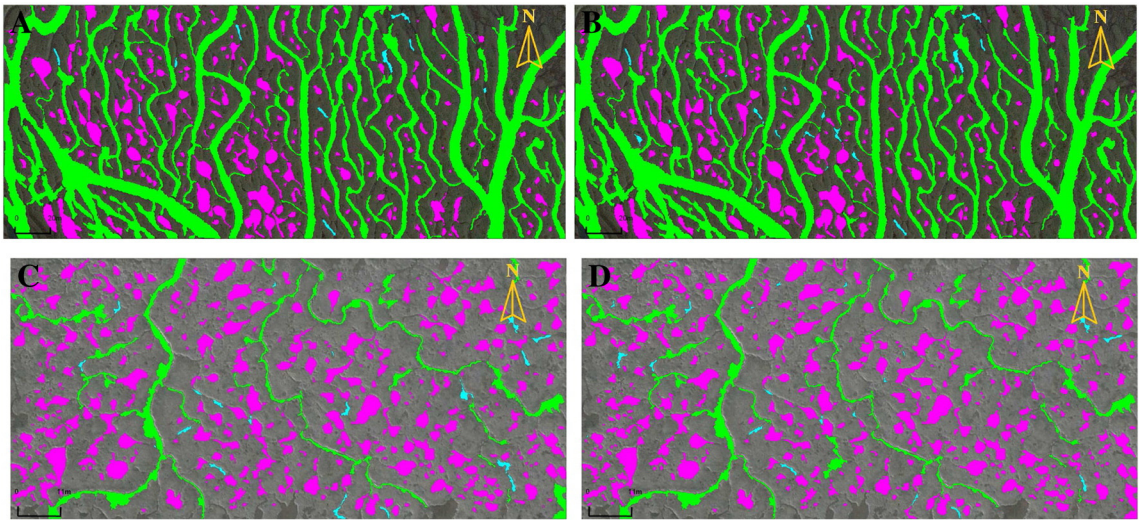

Fig. 8. Classification results in validation zones with their global accuracy. North Bay Zone 8: 7 Supervised classification-$A_g = 100\%$. 7 Automatic classification-$A_g = 91.4\%$. Arcachon Bay Zone 9: 7 Supervised classification-$A_g = 100\%$. 7 Automatic classification-$A_g = 94.5\%$. Pond, Course and Other classes are shown in magenta, green and cyan, respectively.

Table 4
Bahía Blanca Estuary Zone 3 performance: (A) Confusion matrix. (B) Classification results. Bahía Blanca Estuary Zone 4 performance: (C) Confusion matrix. (D) Classification results. Bahía Blanca Estuary Zone 5 performance: (E) Confusion matrix. (F) Classification results.

A

		Predicted		
		Pond	Course	Other
Actual	Pond	381	1	2
	Course	1	27	0
	Other	11	0	16

B

Parameter	Value
A_g[%]	96.6%
R_{Tp}	0.99
R_{Tc}	0.96
R_{To}	0.59
R_{Fp}	0.96
R_{Fc}	0.96
R_{Fo}	0.88
$P_r(a)$	0.96
$P_r(e)$	0.79
κ	0.84

C

		Predicted		
		Pond	Course	Other
Actual	Pond	383	5	5
	Course	0	7	0
	Other	6	1	5

D

Parameter	Value
A_g[%]	95.9%
R_{Tp}	0.97
R_{Tc}	1.00
R_{To}	0.42
R_{Fp}	0.98
R_{Fc}	0.54
R_{Fo}	0.50
$P_r(a)$	0.95
$P_r(e)$	0.90
κ	0.58

E

		Predicted		
		Pond	Course	Other
Actual	Pond	214	0	5
	Course	0	9	0
	Other	4	0	11

F

Parameter	Value
A_g[%]	96.3%
R_{Tp}	0.97
R_{Tc}	1.00
R_{To}	0.73
R_{Fp}	0.98
R_{Fc}	1.00
R_{Fo}	0.69
$P_r(a)$	0.96
$P_r(e)$	0.81
κ	0.80

Table 5
Río Gallegos Estuary Zone 6 performance: (A) Confusion matrix. (B) Classification results. Río Gallegos Estuary Zone 7 performance: (C) Confusion matrix. (D) Classification results. North Bay Zone 8 performance: (E) Confusion matrix. (F) Classification results.

A

		Predicted		
		Pond	Course	Other
Actual	Pond	267	3	19
	Course	0	9	0
	Other	14	0	38

B

Parameter	Value
A_g[%]	89.7%
R_{Tp}	0.92
R_{Tc}	1.00
R_{To}	0.73
R_{Fp}	0.95
R_{Fc}	0.75
R_{Fo}	0.66
$P_r(a)$	0.90
$P_r(e)$	0.67
κ	0.70

C

		Predicted		
		Pond	Course	Other
Actual	Pond	130	0	1
	Course	0	7	0
	Other	3	0	44

D

Parameter	Value
A_g[%]	97.8%
R_{Tp}	0.99
R_{Tc}	1.00
R_{To}	0.94
R_{Fp}	0.98
R_{Fc}	1.00
R_{Fo}	0.98
$P_r(a)$	0.98
$P_r(e)$	0.57
κ	0.95

E

		Predicted		
		Pond	Course	Other
Actual	Pond	194	3	15
	Course	0	13	0
	Other	3	0	15

F

Parameter	Value
A_g[%]	91.4%
R_{Tp}	0.92
R_{Tc}	1.00
R_{To}	0.83
R_{Fp}	0.98
R_{Fc}	0.81
R_{Fo}	0.5
$P_r(a)$	0.91
$P_r(e)$	0.72
κ	0.70

class. The *O* and *P* class shapes have descriptors that tend to be similar, because the *O* class includes the other geographic features that do not purely correspond to ponds or tidal courses for reasons of dynamic sediment.

Finally, Fig. 11 shows the global error in the model classification accuracy. The accuracies obtained are very good for automatic segmentation if it is considered that the classification is made on different features. These geographic features are highly variable in a geomorphological sense.

Table 6
Arcachon Bay Zone 9 performance: (A) Confusion matrix. (A) Classification results.

A

		Predicted		
		Pond	Course	Other
Actual	Pond	331	1	11
	Course	2	19	0
	Other	8	0	29

B

Parameter	Value
A_g[%]	94.5%
R_{Tp}	0.96
R_{Tc}	0.90
R_{To}	0.78
R_{Fp}	0.97
R_{Fc}	0.95
R_{Fo}	0.73
$P_r(a)$	0.94
$P_r(e)$	0.74
κ	0.80

4. Discussion

Using GE images and employing DIP techniques, a morphological data set of ponds and tidal courses characteristics (i.e., box area, form factor, roundness, extent and compactness) is presented, and in turn, an automatic classifier model is provided. The automatic classification of these geographic features tested in different geomorphological settings provide us the resources (information) to investigate their geomorphological processes controlling their formation and evolution in tidal flats environment. In this way, time and costs are considerably reduced.

In general, classification accuracy values A_g are almost optimal in all zones. The mis-classification are associated with other structures (classified as *O* class). This class include the set of connected regions that are not geographic features because they do not purely correspond to ponds or tidal courses for reasons of dynamic sediment. In this sense, the shapes of *O* features may be easily confused with ponds and courses. Considering that our method is tested in different tidal flats environments, there are unbalanced classes between ponds and tidal courses. In this context, pond density is high, so is likely that ponds of different shapes and sizes increase too. This feature variability together with other structures is the reason for mis-classification results. In spite of mis-classification, the accuracy of our method takes these conditions into account because the errors are very low (0.6 and 10.3%). In other words, if there were no *O* class, the model classification would almost be perfect because the shape descriptors used are robust enough to predict the classes. So far, there has been no research that automatically classify these geographic features. For instance, Goudie (2013) characterizes manually the distribution of ponds and courses, and uses a thresholding function in ImageJ software and this also involves spurious structures. In this sense, we compared our output with the threshold image using ImageJ (Fig. 12). The cumulative frequency curves of the original image and our output are analyzed (Fig. 12A). This allow us to find a threshold where both images have the same quantity of pixels. Fig. 12B shows the geographic features (*P*,*C* and *O* classes), the foreground pixels in yellow are the intersection of both images. The red and green foreground pixels correspond to our output and to the threshold image using ImageJ, respectively. In this sense, we can notice that our method is better because the single geographic feature (connected regions) either a pond, a tidal course, or another structure is complete and is different as the thresholding image using ImageJ is. Moreover, in our output the quantity of false positives pixels are reduced and allocate in *O* class. Our accuracy assessment is robust, A_g results obtained in all study sites are higher than 89%. In this sense, the methodology can be easily extrapolated to larger areas obtaining automatically results.

5. Conclusions

Nine zones in different geomorphological settings are characterized by the presence of a large amount of geographic features on their tidal flats. For instance, ponds have a diversity of shapes and origins. An automated classification procedure for these features, able to perform over remote sensing images of large geographical extensions, is a valuable asset in geomorphological studies of these areas. In this work we presented a methodology for such a classification. Only a few supervised learning zones are required to train an unsupervised classifier able to identify ponds and tidal

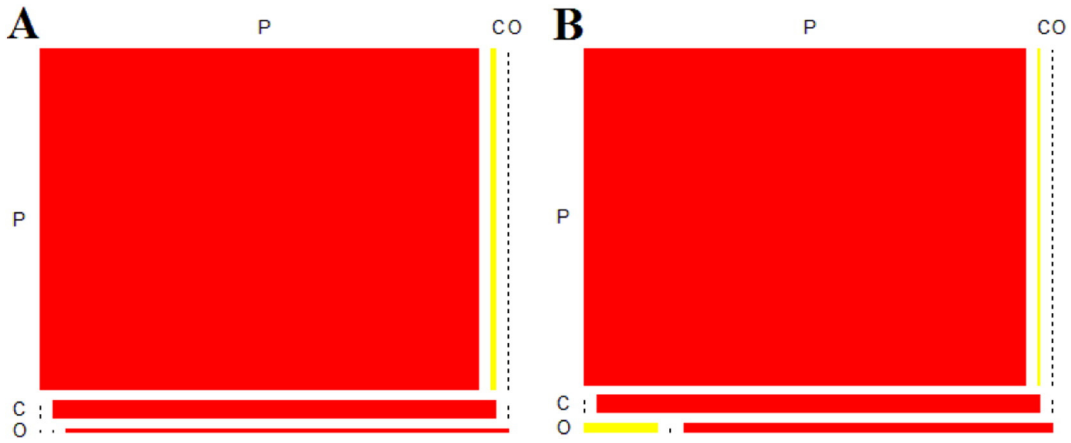

Fig. 9. Confusion matrix mosaic plots. Hits are represented in red and misses in yellow, with areas proportional to the amount of cases: Ponds (P), tidal courses (C) and other structures (O), respectively. Values equal to zero and less than 1% are displayed as a dashed line and a continuous line, respectively. Bahía Blanca Estuary training zones (A) Zone 1 and (B) 2. (For interpretation of the references to color in this figure legend, the reader is referred to the web version of this article.)

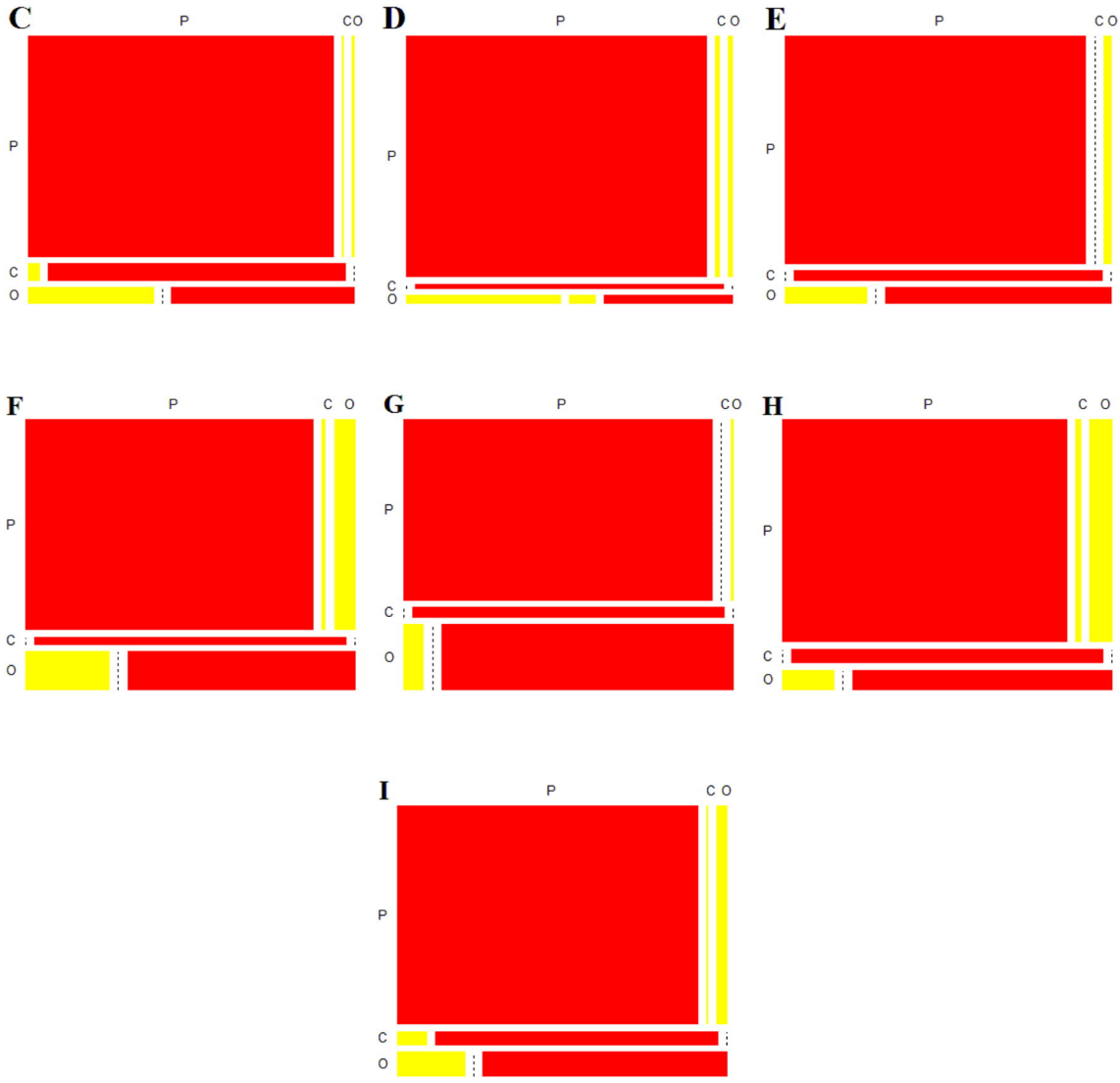

Fig. 10. Confusion matrix mosaic plots. Hits are represented in red and misses in yellow, with areas proportional to the amount of cases: Ponds (P), tidal courses (C) and other structures (O), respectively. Values equal to zero and less than 1% are displayed as a dashed line and a continuous line, respectively. Validation zones (A) Zone 3. (B) Zone 4. (C) Zone 5. (D) Zone 6. (E) Zone 7. (F) Zone 8 and (G) Zone 9. (For interpretation of the references to color in this figure legend, the reader is referred to the web version of this article.)

courses in these images. The processing pipeline developed consists on a segmentation stage (performed in YIQ color space) and a classification stage (using several shape descriptors). The parameters of the unsupervised classifier are obtained by means of a multinomial regression model that adjusts the classification coefficients using the supervised training data. To test the significance of this methodology, we applied the classification to 3 zones in the same estuary that we used to train the classifier, and to other 4 zones in other bays and estuaries worldwide. The quality of the results, in terms of classification accuracy and consensus, appear to be quite significant.

This study could be considered as a preliminary analysis in automatic classification, identification and measurement of ponds and tidal courses in tidal flats using available Google Earth images. However, the methodology can be employed in any kind of image. Its main advantage (unsupervised methods) is that human intervention is only used for the interpretation of the obtained data, thus minimizing cost and time. In general, the developed pipeline of the methodology is automatic, the user intervention is required only at the stage of segmentation where the user determines the number of prototype pixels required to separate background and foreground.

The results have high accuracy in the automatic classification of each feature regardless the zones locations. These preliminary results open several lines of research. Among them is the study of various geomorphological processes and the development of a predictive model in decision-making. For instance, in restoration sites, where pond and tidal creek construction projects are necessary in estuarine wetlands (Brand et al., 2012; Shih et al., 2015). Furthermore, the study of each geographic feature behavior and evolution inside its own environment may be also addressed.

Acknowledgments

Financial support for this research was provided by grants from ANPCYT, CONICET and UNS. Further information about the methodology can be obtained from either the Sr. author, CAD or GMEP. We wish to thank both reviewers for their constructive comments and suggestions that greatly improve of the manuscript.

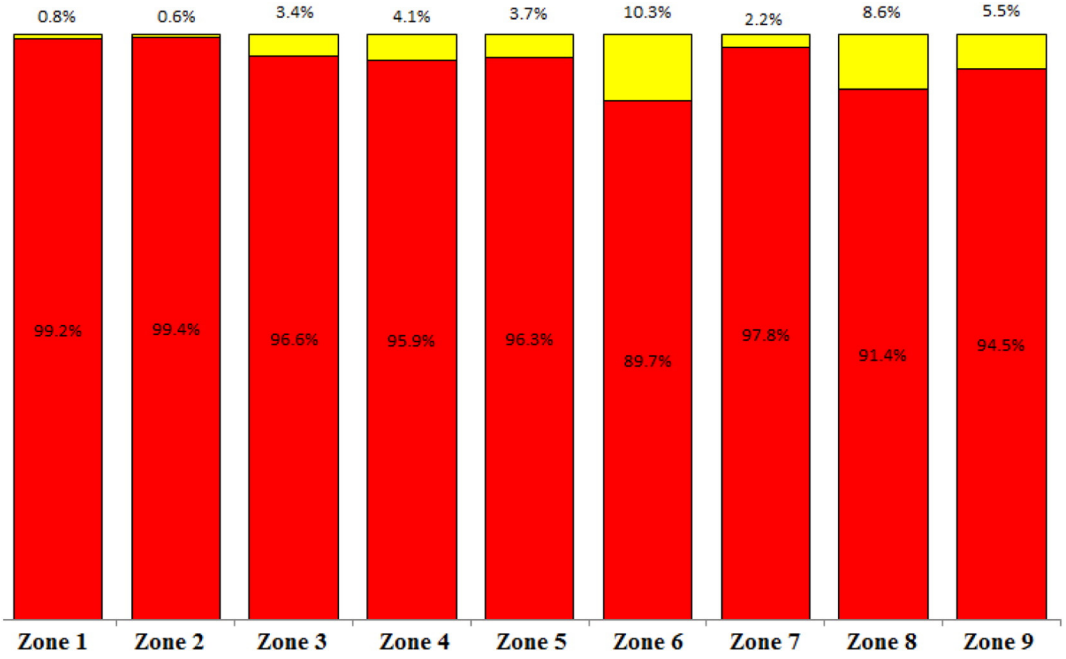

Fig. 11. Global error of automatic classification in each study zone.

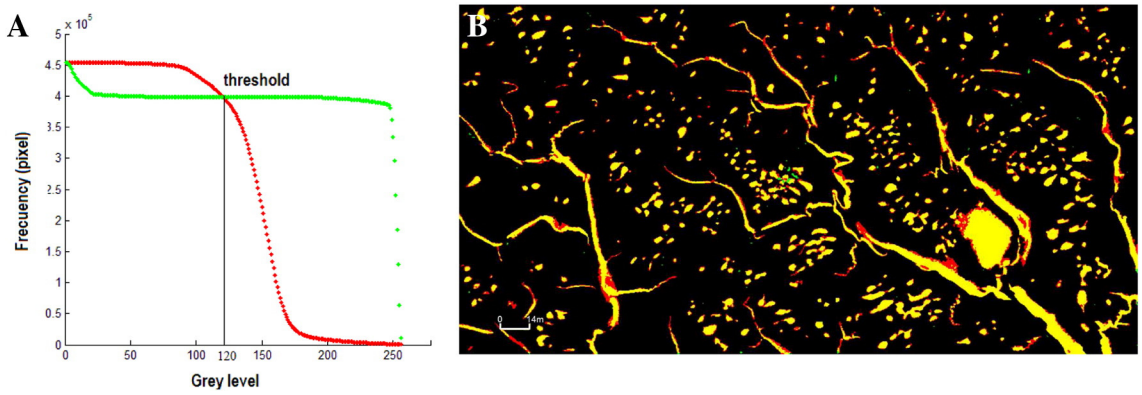

Fig. 12. Comparison between our binary image and the threshold image using ImageJ. (A) Cumulative frequency curves of the original image and our segmentation image in red and green, respectively. (B) The output of join both thresholding, using our methodology (red foreground pixels) and ImageJ (green foreground pixels). (For interpretation of the references to color in this figure legend, the reader is referred to the web version of this article.)

References

Agresti, A., 1996. An Introduction to Categorical Data Analysis. second ed Wiley-Interscience, New Jersey.

Boston, K.G., 1983. The development of salt pans on tidal marshes, with particular reference to South-Eastern Australia. J. Biogeogr. 10, 1–10.

Brand, L.A., Smith, L.M., Takekawa, J.Y., Athearn, N.D., Taylor, K., Shellenbarger, G.G., Schoellhamer, D.H., Spenst, R., 2012. Trajectory of early tidal marsh restoration: elevation, sedimentation and colonization of breached salt ponds in the northern San Francisco Bay. Ecol. Eng. 42, 19–29.

Campbell, J., 2002. Introduction to Remote Sensing. second ed The Guilford Press, New York.

Chapman, V.J.V.J., 1960. Salt Marshes and Salt Deserts of the World/by V. J. Chapman. L. Hill, London (New York: Interscience Publishers).

Cipolletti, M.P., Delrieux, C.A., Perillo, G.M.E., Piccolo, M.C., 2012. Superresolution border segmentation and measurement in remote sensing images. Comput. Geol. 40, 87–96. http://dx.doi.org/10.1016/j.cageo.2011.07.015.

Cipolletti, M.P., Delrieux, C.A., Perillo, G.M.E., Piccolo, M.C., 2014. Border extrapolation using fractal attributes in remote sensing images. Comput. Geosci. 62, 25–34.

Cohen, J., 1960. A coefficient of agreement for nominal scales. Educ. Psychol. Meas. 20, 37–46. http://dx.doi.org/10.1177/001316446002000104.

Congalton, R.G., 1991. A review of assessing the accuracy of classifications of remotely sensed data. Remote Sens. Environ. 37, 35–46.

Congalton, R.G., Green, K., 2008. Assessing the Accuracy of Remotely Sensed Data: Principles and Practices. CRC press, Boca Raton.

Escapa, M., Perillo, G.M.E., Iribarne, O., 2015. Biogeomorphically driven salt pan formation in Sarcocornia-dominated salt-marshes. Geomorphology 228, 147–157.

Fleiss, J.L., 1981. Statistical Methods for Rates and Proportions. second ed Wiley & Sons, New York.

Foody, G.M., 2002. Status of land cover classification accuracy assessment. Remote Sens. Environ. 80, 185–201.

Franklin, S., Peddle, D., Dechka, J., Stenhouse, G., 2002. Evidential reasoning with Landsat TM, DEM and GIS data for landcover classification in support of grizzly bear habitat mapping. Int. J. Remote Sens. 23, 4633–4652.

Frey, R., 1985. Coastal and salt marshes. Coast. Sediment. Environ. 187–224.

Friedman, H., Rubin, J., 1967. On some invariant criteria for grouping data. J. Am. Stat. Assoc. 62, 1159–1178.

Friendly, M., 1994. Mosaic displays for multi-way contingency tables. J. Am. Stat. Assoc. 89, 190–200.

Friess, D.A., Kudavidanage, E.P., Webb, E.L., 2011. The digital globe is our oyster. Front. Ecol. Environ. 9, 542.

Gallego, F.J., 2004. Remote sensing and land cover area estimation. Int. J. Remote Sens. 25, 3019–3047.

Girard, C.M., Girard, M.C., 1999. Processing of Remote Sensing Data. Dunod, Paris.

Goudie, A., 2013. Characterising the distribution and morphology of creeks and pans on salt marshes in England and Wales using Google Earth. Estuar. Coast. Shelf Sci. 129, 112–123.
Haralick, R.M., Kelly, G.L., 1969. Pattern recognition with measurement space and spatial clustering for multiple images. Proc. IEEE 57, 654–665. http://dx.doi.org/10.1109/PROC.1969.7020.
Hartigan, J.A., Kleiner, B., 1981. Mosaics for Contingency Tables. In: Eddy, W.F. (Ed.), Computer Science and Statistics: Proceedings of the 13th Symposium on the Interface. Springer, US, pp. 268–273.
Hosmer, D.W., Lemeshow, S., 2000. Applied Logistic Regression. second ed Wiley & Sons, Inc., New Jersey.
Jr, P., Gilmore, R., Millones, M., 2011. Death to Kappa: birth of quantity disagreement and allocation disagreement for accuracy assessment. Int. J. Remote Sens. 32, 4407–4429.
Lillesand, T., Kiefer, R., Chipman, J., 2004. Remote Sensing and Image Interpretation. fifth ed Willey & Sons, New York.
Lunetta, R.S., Lyon, J.G., 2004. Remote Sensing and GIS Accuracy Assessment. CRC press, Boca Raton.
Minkoff, D., Escapa, M., Ferramola, F., Maraschn, S., Pierini, J., Perillo, G.M.E., Delrieux, C., 2006. Effects of crab–halophytic plant interactions on creek growth in a SW Atlantic salt marsh: a cellular automata model. Estuar. Coast. Shelf Sci. 69, 403–413.
Packham, J.R., Liddle, M.J., 1970. The Cefni salt marsh, Anglesey, and its recent development. Field Stud. 3, 331–356.
Pal, M., Mather, P.M., 2003. An assessment of the effectiveness of decision tree methods for land cover classification. Remote Sens. Environ. 86, 554–565.
Perillo, G.M.E., GarcÃa Martínez, M., Piccolo, M.C., 1996. Geomorfología de canales de marea: análisis de fractales y espectral. Actas VI Reun. Argent. Sedimentol. 155–160.
Perillo, G.M.E., 2009. Tidal Courses: Classification, Origin and Functionality. Coastal Wetlands, An Integrated Ecosystem Approach, Elsevier, Amsterdam, pp. 185–209.
Perillo, G.M.E., Iribarne, O.O., 2003. New mechanisms studied for creek formation in tidal flats: from crabs to tidal channels. *EOS Trans. Am. Geophys. Union* 84, 1–5.
Perillo, G., Wolanski, E., Cahoon, D., Brison, M., 2009. Coastal Wetlands, An Integrated Ecosystem Approach. Elsevier Science, Netherlands.
Pethick, J.S., 1974. The distribution of salt pans on tidal salt marshes. J. Biogeogr. 1, 57–62.
Richards, J.A., Jia, X., 2006. Remote Sensing Digital Image Analysis: An Introduction. Springer, Berlin.
Russ, J.C., 1999. The Image Processing Handbook. third ed. CRC Press, Boca Raton, FL.
Saha, S., Bandyopadhyay, S., 2010. Application of a multiseed-based clustering technique for automatic satellite image segmentation. IEEE Geosci. Remote Sens. Lett. 7, 306–308.
Shih, S.-S., Hwang, G.-W., Hsieh, H.-L., Chen, C.-P., Chen, Y.-C., 2015. Geomorphologic dynamics and maintenance following mudflat, creek and pond formation in an estuarine mangrove wetland. Ecol. Eng. 82, 590–595.
Sridhar, P.N., Surendran, A., Ramana, I.V., 2008. Auto-extraction technique-based digital classification of saltpans and aquaculture plots using satellite data. Int. J. Remote Sens. 29, 313–323.
Steers, J.A., 1964. The Coastline of England and Wales. Cambridge Univ. Press, Reidel, Dordrecht.
Wilkinson, G.G., 2005. Results and implications of a study of fifteen years of satellite image classification experiments. IEEE Trans. Geosci. Remote Sens. 43, 433–440.
Yapp, R.H., Johns, D., Jones, O.T., 1917. The salt marshes of the dovey estuary. J. Ecol. 5, 65–103.
Yu, L., Gong, P., 2012. Google Earth as a virtual globe tool for Earth science applications at the global scale: progress and perspectives. Int. J. Remote Sens. 33, 3966–3986.
Zular, A., Guedes, C.C.F., Mendes, V.R., Sawakuchi, A.O., Giannini, P.C.F., Tanaka, A.P.B., Fornari, M., Nascimento, D.R., 2012. Geomorphological analysis of coastal depositional systems in SE Brazil aided by Google Earth coupled with the integration of chronological and sedimentological data by means of a Google Fusion Table. Geol. Soc. Am. Spec. Pap. 492, 113–125.